

## Article

# Closed-Form DoA Solution for Co-Centered Orthogonal Microphone Arrays Based on Multilateration Equations

Kazım Zengin <sup>1,\*</sup>  and Aydın Yeşildirek <sup>2</sup> <sup>1</sup> Department of Mechatronics Engineering, Kırklareli University, Kırklareli 39100, Turkey<sup>2</sup> Department of Mechatronics Engineering, Yıldız Technical University, Istanbul 34349, Turkey; aydiny@yildiz.edu.tr

\* Correspondence: kazim.zengin@klu.edu.tr

**Abstract:** This study proposes a closed-form direction-of-arrival (DoA) solution derived from multilateration equations for microphone arrays of co-centered and orthogonal pairs. The generalized cross-correlation phase transform (GCC-Phat) algorithm is used to obtain the time-difference-of-arrival (TDoA) values. Simulation studies have shown the success of our proposed method compared to existing DoA methods in the literature by varying the sampling frequency of the sound signal, inter-microphone distances, and the source distance. The results from the simulation are validated by the measurements from our experiments. Our proposed solution gives better results than the far-field solution against the angle error, which is more pronounced at incidence angles smaller than 15°. These angle errors, which approach 3° using the far-field method, are reduced to less than 0.5 degrees using our proposed solution. Our solution also gives more stable results against TDoA measurement errors. Our proposed solution achieves a 66% improvement for azimuth angle and 5.88% improvement for elevation angle compared to the simulation results in the absence of TDoA measurement error, outperforming the far-field approach. When normally distributed sampling error is added to TDoA measurements, with a standard deviation of three samples, our proposed solution achieves a 41% improvement for azimuth angle and a 5.44% improvement for elevation angle. In our field measurements, an absolute mean error of 0.94 degrees was observed with our proposed method for azimuth angle. It is shown to be a more stable and faster solution method for real-time applications.



**Citation:** Zengin, K.; Yeşildirek, A. Closed-Form DoA Solution for Co-Centered Orthogonal Microphone Arrays Based on Multilateration Equations. *Appl. Sci.* **2023**, *13*, 11297. <https://doi.org/10.3390/app132011297>

Academic Editor: Jie Tian

Received: 7 September 2023

Revised: 2 October 2023

Accepted: 11 October 2023

Published: 14 October 2023



**Copyright:** © 2023 by the authors. Licensee MDPI, Basel, Switzerland. This article is an open access article distributed under the terms and conditions of the Creative Commons Attribution (CC BY) license (<https://creativecommons.org/licenses/by/4.0/>).

**Keywords:** multilateration; DoA estimation; sound source localization; acoustic localization; microphone array

## 1. Introduction

Acoustic DoA estimation is a common technique used in a variety of applications, including indoor security systems, conference speaker tracking systems, mobile robot positioning systems, outdoor security systems, and defense industry systems. DoA estimation is performed by using microphone arrays with predefined distances between the microphones. The accuracy and speed of DoA estimation directly affects the performance of the systems.

Sound localization methods can be divided into two categories: direct and indirect methods. Direct methods estimate the position of a sound source in a single step, while indirect methods estimate the position of a sound source by calculating the TDoA times between microphones and then using the known microphone array geometry [1]. Direct methods are divided into two main classes: spectral-based and beamformer-based approaches. The first class consists of studies that directly locate by filtering, weighting, and summing the signals received from the microphone. The maximization of the steered response power of a beamformer forms the basis of this class, and SRP-PHAT [2] is the most widely used method in this class [3,4]. The second class includes applications of high-resolution spectral

estimation based on the signal correlation matrix. The most widely used methods in this class are MUSIC [5] and ESPRIT [6]. Indirect methods include approaches that perform location estimation based on the TDoA information between microphones [7–9]. In recent years, there has been a development of deep learning-based methods as well [10–12].

Direct localization methods are frequently used in applications where the location of the sound is known and the sound source is one of the multiple candidate sound sources. These methods are computationally demanding. The direction of arrival (DoA) of a sound source with unknown location and whose distance to the reference point of the microphone array is much greater than the inter-microphone distance of the microphone array is calculated using the far-field approach. In the far-field approach, it is assumed that the sound waves propagate to the microphones in parallel lines [1,13]. It is frequently utilized to detect the DoA of sound sources with unknown locations. The far-field approach method uses TDoA times between microphones. The most frequently used method in the literature for obtaining TDoA values is the GCC method, which uses the PHAT weighting function [14]. The details of the method will not be explained in this paper.

If the distance value between the sound source and the reference point of the microphone array is close to the distance value between the microphones, the sound source can be localized using the triangulation method or the multilateration method using the TDoA values [15–18]. In the model used to detect the location of weapons that can fire ammunition with a Mach number greater than one, the distance can be estimated using the angle of arrival and the time difference between the shock wave and the muzzle burst, and the location can thus be determined [19].

Although different microphone geometries have been used in studies, uniform linear (ULA) [13] and uniform circular (UCA) [20] distributed, L-shaped, and spherical microphone arrays are more common. Among these microphone arrays, the L-shaped [21,22] microphone arrays and the circular [3,23], spherical [24–27], and spatial [23] microphone arrays with a multiple of four co-dispersed microphones in the same plane have co-centered and orthogonal pairs of microphones.

This study presents closed-form azimuth and elevation angle solutions for microphone arrays with co-centered and orthogonally placed microphone pairs using TDoA times. The obtained solution provides accurate angle and quadrant estimation in a single step using the same microphone array geometry as in the far-field approach. Additionally, in our simulation studies, it is observed that the zero-angle error in the far-field approach can be reduced to near-zero values with the proposed method with appropriate microphone aperture and more accurate results are produced against TDoA measurement errors. The success of our method is demonstrated with the experimental results.

The paper is organized as follows: In Section 2, we review the existing DoA methods based on the far-field approach and explain the multilateration method. In Section 3, we explain the observation that forms the basis of the solution we obtained. Then, we obtain the arrival angle detection method we propose from the multilateration equations. In Section 4, we report the simulation results of the proposed method with the existing methods. In Section 5, we report the experimental study and the results obtained. In the final section, we discuss the success of the proposed method compared to the existing methods and conclude the paper.

## 2. General Properties of Method

The azimuth and elevation angles of a point defined with respect to the origin in three-dimensional space are shown in Figure 1. The azimuth and elevation angles of the  $\mathbf{p}_k$  vector with known coordinates are therefore as follows:

$$\theta = \text{atan2}(y_k, x_k) \quad (1)$$

$$\varphi = \text{atan2}\left(z_k, \sqrt{x_k^2 + y_k^2}\right) \quad (2)$$

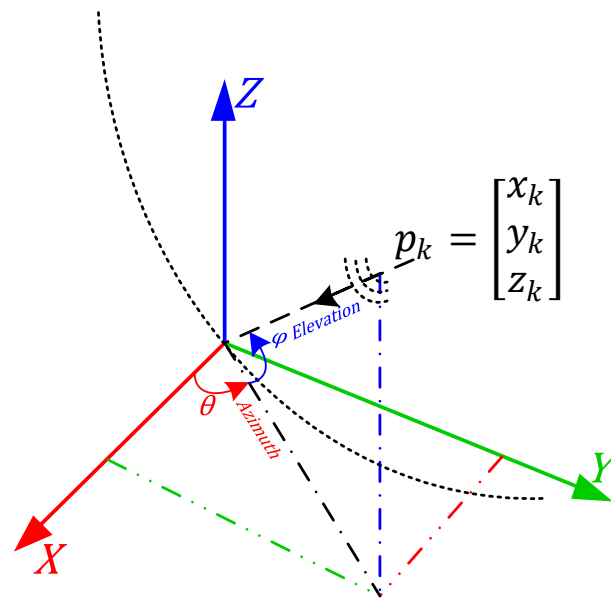


**Figure 1.** The azimuth ( $\theta$ ) and elevation ( $\varphi$ ) angles of a vector defined in Cartesian space.

The elevation angle of a  $p_k$  vector defined in a plane is zero.

2.1. Far-Field Approximation

The model for detecting an explosion sound occurring at a distance of  $d_k$  using a sensor array consisting of microphones placed at intervals of  $d_m$  is illustrated in Figure 2, where  $d_k$ : the distance of the source to the origin,  $d_i$ : the distance vector of the source to  $m_i$ , and  $d_m$ : distance vector between  $m_1$  and  $m_2$  and observe that  $\vec{d}_1 = \vec{d}_2 + \vec{d}_m$ .

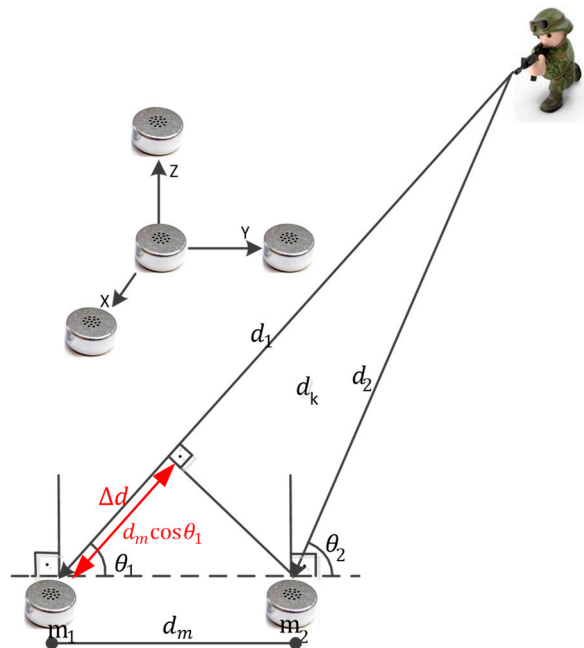


**Figure 2.** Direction-of-arrival (DoA) estimation and microphone array structure.

In the case where  $d_k \gg d_m$ , the sound wave is assumed to propagate as a linear beam ( $\theta_1 = \theta_2$ ). Therefore, with  $v_s$  being the speed of sound, the distance difference ( $\Delta d$ ) and the DoA that form the time delay between the microphones ( $\tau_{12}$ ) are given:

$$\Delta d = v_s \times \tau_{12} \tag{3}$$

$$\theta_1 = \text{acos}\left(\frac{v_s \times \tau_{12}}{d_m}\right) \tag{4}$$

When the DoA is calculated with two microphones, two symmetrical angle values are obtained along the direction of the microphones. To avoid this, a third microphone is placed perpendicular to the direction of the two microphones, as shown in Figure 3a. The result obtained with the other two microphones also produces two angle values. However, the intersection of the two solutions gives the correct angle of arrival. If the elevation angle is also to be calculated, a fourth microphone is placed perpendicular to the plane formed by the three microphones, as shown in Figure 3b, and both the lateral and elevation angles are detected, but the distance cannot be estimated [28].

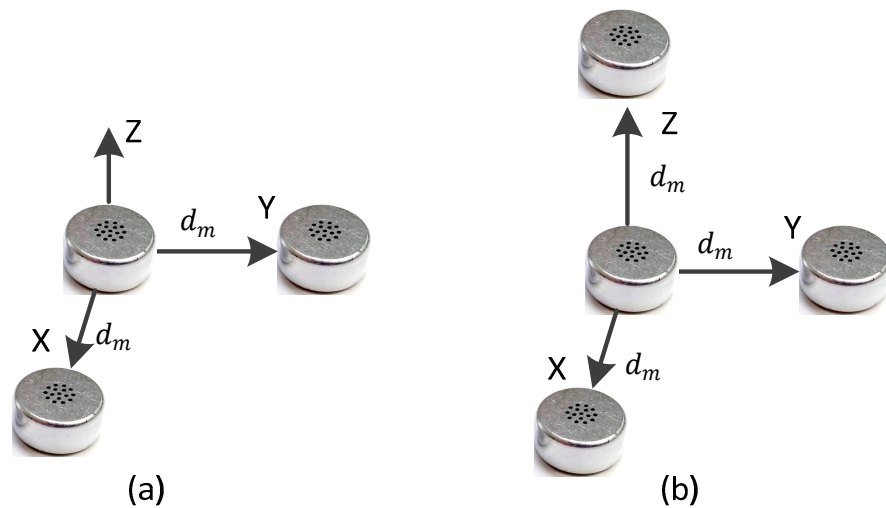


**Figure 3.** (a) Microphone array utilized in the plane and (b) microphone array utilized in the Cartesian space.

In one study, the origin was considered to be the midpoint of the microphones shown in Figure 2, the DoA was calculated relative to the origin, and the half scale of the right triangle obtained in Figure 2 was used to model it [29]. According to this model, the DoA formula is given by Parsayan and Ahadi as follows:

$$\theta = 90 - \text{acos}\left(\sqrt{1 - \left(\frac{v_s \times \tau_{12}}{d_m}\right)^2}\right) \tag{5}$$

### 2.2. Multilateration Method

In order to perform localization in a two-dimensional Cartesian plane, a sensor array consisting of at least three microphones placed at different positions is required. For the three-microphone sensor array shown in Figure 3a, let the planar position of the microphones be denoted by  $p_i = [x_i, y_i]^T$ ,  $i = 1, 2, 3$  and the position of the sound source be denoted by  $p_k = [x_k, y_k]^T$ .

Let us denote the arrival times of sound signals at the microphones as  $\tau_i$  and the time difference between the arrivals at two microphones as  $\tau_{ij} = \tau_i - \tau_j$ . In this case, the

distance between the sound source and the microphones, depending on the speed of sound propagation in the air, is given as follows:

$$d_i = \|\mathbf{p}_k - \mathbf{p}_i\| = \tau_i \times v_s \tag{6}$$

Therefore, the distance between the  $i$ -th microphone and the source is as follows:

$$d_i = \sqrt{(x_k - x_i)^2 + (y_k - y_i)^2} \tag{7}$$

By taking the first microphone as a reference, we can write Equation (6) for the  $j$ -th microphone and the reference microphone, and then take the difference and rearrange as follows:

$$\tau_{j1} \times v_s = \|\mathbf{p}_k - \mathbf{p}_j\| - \|\mathbf{p}_k - \mathbf{p}_1\| \tag{8}$$

By squaring both sides of Equation (8), we obtain the following:

$$\tau_{j1}^2 \times v_s^2 + \|\mathbf{p}_k - \mathbf{p}_1\|^2 + 2 \times v_s \times \tau_{j1} \times \|\mathbf{p}_k - \mathbf{p}_1\| = \|\mathbf{p}_k - \mathbf{p}_j\|^2 \quad j = 2, 3, \dots, N \tag{9}$$

With the expansion of the quadratic expressions formed in Equation (9):

$$\tau_{j1}^2 \times v_s^2 + \mathbf{p}_k^T \mathbf{p}_k - 2\mathbf{p}_1^T \mathbf{p}_k + \mathbf{p}_1^T \mathbf{p}_1 + 2 \times v_s \times \tau_{j1} \times \|\mathbf{p}_k - \mathbf{p}_1\| = \mathbf{p}_k^T \mathbf{p}_k - 2\mathbf{p}_j^T \mathbf{p}_k + \mathbf{p}_j^T \mathbf{p}_j \tag{10}$$

By performing the necessary simplifications in Equation (10), and by moving the unknowns to the left-hand side of the equation and the knowns to the right-hand side, we obtain the following:

$$2\mathbf{p}_j^T \mathbf{p}_k - 2\mathbf{p}_1^T \mathbf{p}_k + 2 \times v_s \times \tau_{j1} \times \|\mathbf{p}_k - \mathbf{p}_1\| = \mathbf{p}_j^T \mathbf{p}_j - \mathbf{p}_1^T \mathbf{p}_1 - \tau_{j1}^2 \times v_s^2 \tag{11}$$

By substituting the distance between the reference microphone and the sound source,  $d_1 = \|\mathbf{p}_k - \mathbf{p}_1\|$ , into Equation (11):

$$2\mathbf{p}_j^T \mathbf{p}_k - 2\mathbf{p}_1^T \mathbf{p}_k + 2 \times v_s \times \tau_{j1} \times d_1 = \mathbf{p}_j^T \mathbf{p}_j - \mathbf{p}_1^T \mathbf{p}_1 - \tau_{j1}^2 \times v_s^2 \quad j = 2, 3, \dots, N \tag{12}$$

The linear equation between the first microphone, which is taken as the reference, and the  $j$ -th microphone, with  $\mathbf{p}_k$  and  $d_1$  as unknowns, is defined in Equation (12). For  $N$  microphones,  $N - 1$  equations are written using the same reference microphone. For a sensor array shown in Figure 3a, the equations are rearranged as follows:

$$\begin{bmatrix} 2(\mathbf{p}_2 - \mathbf{p}_1)^T & 2v_s\tau_{21} \\ 2(\mathbf{p}_3 - \mathbf{p}_1)^T & 2v_s\tau_{31} \end{bmatrix} \times \begin{bmatrix} \mathbf{p}_k \\ d_1 \end{bmatrix} = \begin{bmatrix} \mathbf{p}_2^T \mathbf{p}_2 - \mathbf{p}_1^T \mathbf{p}_1 - v_s^2 \tau_{21}^2 \\ \mathbf{p}_3^T \mathbf{p}_3 - \mathbf{p}_1^T \mathbf{p}_1 - v_s^2 \tau_{31}^2 \end{bmatrix} \tag{13}$$

The general solution can be obtained by writing Equation (13) as a matrix equation:

$$\mathbf{A} \mathbf{x} = \mathbf{b} \tag{14}$$

with  $\mathbf{A} \in \mathbb{R}^{(N-1) \times 4}$ ,  $\mathbf{b} \in \mathbb{R}^{(N-1)}$  and  $\mathbf{x} \in \mathbb{R}^4$ . The  $(i - 1)$ -th rows of the matrices  $\mathbf{A}$  and  $\mathbf{b}$ , for  $i = 2, 3, \dots, N$ :

$$\mathbf{a}_{i-1} = [2(\mathbf{p}_i - \mathbf{p}_1)^T \quad 2v_s\tau_{i1}], \mathbf{b}_{i-1} = [\mathbf{p}_i^T \mathbf{p}_i - \mathbf{p}_1^T \mathbf{p}_1 - v_s^2 \tau_{i1}^2]$$

When a sufficient number of microphone measurements are taken (i.e.,  $\mathbf{A}^T \mathbf{A}$  is a full-rank matrix), the unknown  $\mathbf{x}$  solution can be obtained using the LSE method [30]:

$$\begin{bmatrix} \mathbf{p}_k \\ d_1 \end{bmatrix} = (\mathbf{A}^T \mathbf{A})^{-1} \mathbf{A}^T \mathbf{b} \tag{15}$$

When Equation (13) is examined, it is evident that the matrix  $A$  and the vector  $b$  are dependent on the TDoA values. Therefore, the accuracy of the method in producing results close to the true location depends on the correct determination of the TDoA values.

### 3. Applications

The multilateration method was investigated in MATLAB simulations by considering different source distances, sampling frequencies, arrival angles, and microphone spacings. In the simulations, a microphone array consisting of five microphones, one in the center and four arranged in a circle, was used. The Equation (13) was arranged for five microphones by considering the center microphone as the reference. The model we created for the TDoA time between two microphones in the simulations is shown in Figure 4.

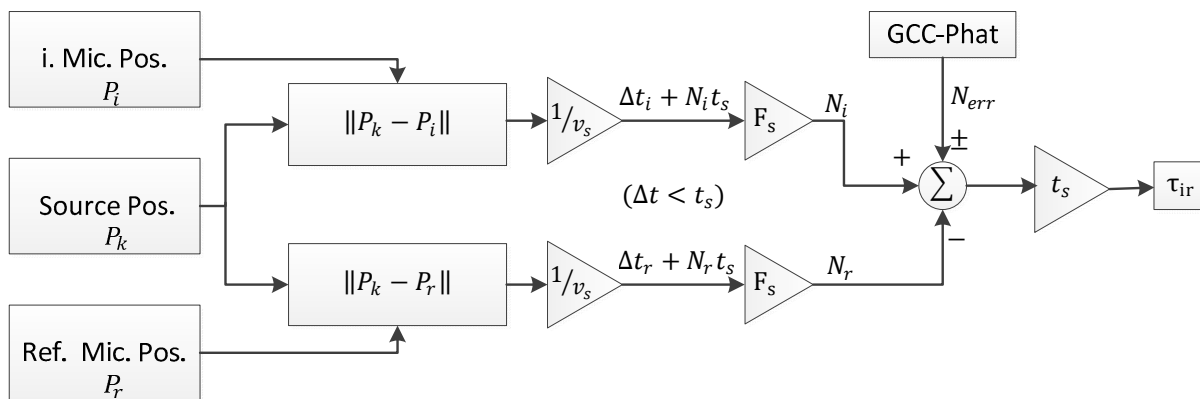


Figure 4. The TDoA model used in simulation studies.

The TDoA model specifies that the  $N_i$  and  $N_r$  values represent the number of samples that will be formed until the sound reaches the  $i$ . and the reference microphones, respectively, after it is formed.  $N_{err}$  is the amount of error that the GCC-Phat algorithm will produce due to environmental noise added to the source sound in real-time applications. The time  $\Delta t$  is the unmeasured time at which the sound arrives at the microphones, which, depending on the sampling frequency, is less than the sampling time  $t_s$ .  $\Delta t_i$  and  $\Delta t_r$  are the unmeasured times at which the sound reaches microphone  $i$  and the reference microphone, respectively. In our simulation study, the sound source, which is assumed to be 150 m away, was examined at five different angles of  $0^\circ$ ,  $-30^\circ$ ,  $-45^\circ$ ,  $-60^\circ$ , and  $-90^\circ$ . The distance  $d_m$  between the microphones was increased from 0.5 m to 3 m in 0.5 m steps. In the simulation study, the sampling frequency  $F_s$  was set to 44.1 kHz. In Figure 5, the LSE solutions obtained by solving Equation (15) for each  $d_m$  distance are shown as “\*”, and the actual source position is shown as “o”. It can be observed that the location estimates approach the actual location value as the microphone spacing is increased.

#### 3.1. Origin of the Idea and Proposed Method

An analysis of Figure 5 shows that  $d_m$  is insufficient for accurate location estimation, and that the location estimates change along the same line, even with high estimation errors. This observation suggests that the DoA estimation based on the multilateration method can be performed with high accuracy, independent of  $d_m$ .

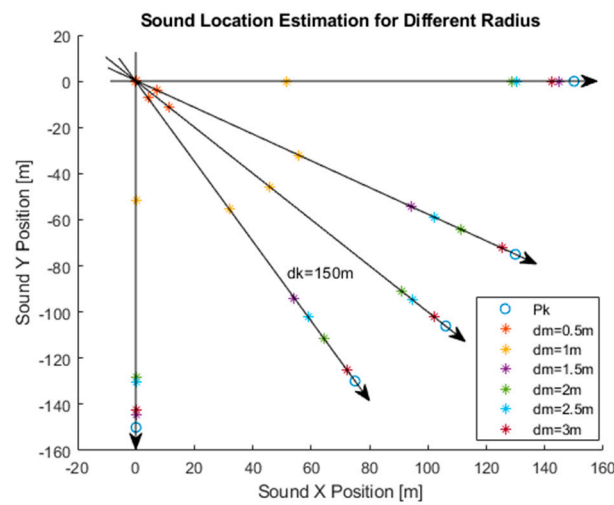


Figure 5. Localization of a sound source located at five different angles at a distance of 150 m by using different  $d_m$  distances.

The multilateration equations for a microphone array consisting of three microphones, with the first microphone as the reference, are shown in Equation (13). Assuming that the distance from the sound source to the first microphone,  $d_1$ , is known, Equation (13) can be rearranged as follows:

$$\begin{bmatrix} 2(\mathbf{p}_2 - \mathbf{p}_1)^T \\ 2(\mathbf{p}_3 - \mathbf{p}_1)^T \end{bmatrix} \times [\mathbf{p}_k] = \begin{bmatrix} \mathbf{p}_2^T \mathbf{p}_2 - \mathbf{p}_1^T \mathbf{p}_1 - v_s \tau_{21} (v_s \tau_{21} + 2d_1) \\ \mathbf{p}_3^T \mathbf{p}_3 - \mathbf{p}_1^T \mathbf{p}_1 - v_s \tau_{31} (v_s \tau_{31} + 2d_1) \end{bmatrix} \quad (16)$$

The simple representation of Equation (16) is as follows:

$$\mathbf{A}_1 \mathbf{x}_1 = \mathbf{b}_1 \quad (17)$$

To perform localization on the plane, the distances of the microphones located on the perpendicular axes in the sensor array shown in Figure 3a to the reference microphone are taken as  $d_{mx}$  and  $d_{my}$ . Since the reference microphone is located at the origin,  $d_1 = d_k$ . According to these, the  $\mathbf{A}_1$  matrix is as follows:

$$\mathbf{A}_1 = 2 \times \begin{bmatrix} d_{mx} & 0 \\ 0 & d_{my} \end{bmatrix} \quad (18)$$

$\mathbf{b}_1$  vector:

$$\mathbf{b}_1 = \begin{bmatrix} d_{mx}^2 - v_s^2 \times \tau_{21}^2 - 2v_s \tau_{21} d_k \\ d_{my}^2 - v_s^2 \times \tau_{31}^2 - 2v_s \tau_{31} d_k \end{bmatrix} \quad (19)$$

If we consider that the second microphone is on the  $x$ -axis and the third microphone is on the  $y$ -axis, we can write  $\tau_{21} = \tau_x$  and  $\tau_{31} = \tau_y$ . It is clear that  $-d_{mx} \leq v_s \tau_x \leq d_{mx}$  and  $-d_{my} \leq v_s \tau_y \leq d_{my}$ , depending on the direction of sound arrival. Therefore, the  $\mathbf{b}_1$  vector can be divided into two components and arranged as

$$\mathbf{b}_1 = \underbrace{\begin{bmatrix} d_{mx}^2 - v_s^2 \times \tau_x^2 \\ d_{my}^2 - v_s^2 \times \tau_y^2 \end{bmatrix}}_{\in \begin{pmatrix} [0, d_{mx}^2] \\ [0, d_{my}^2] \end{pmatrix}} - \begin{bmatrix} 2v_s \tau_x d_k \\ 2v_s \tau_y d_k \end{bmatrix} \quad (20)$$

The first component in Equation (20) is neglected, because it has a very small value compared to the second component. Therefore, Equation (16) can be approximated as follows:

$$\begin{bmatrix} d_{mx} & 0 \\ 0 & d_{my} \end{bmatrix} \times \begin{bmatrix} x_k \\ y_k \end{bmatrix} \approx -v_s d_k \begin{bmatrix} \tau_x \\ \tau_y \end{bmatrix} \tag{21}$$

The  $\mathbf{p}_k$  position vector can be isolated from Equation (21) as follows:

$$\begin{bmatrix} x_k \\ y_k \end{bmatrix} \approx -v_s d_k \begin{bmatrix} \frac{\tau_x}{d_{my}} \\ \frac{d_{mx}}{d_{my}} \end{bmatrix} \tag{22}$$

As shown in Equation (22), the position vector of the sound source varies according to the TDoA values between the microphones. When the ratio of the  $x_k$  and  $y_k$  positions specified in Equation (1) is calculated according to Equation (22), it is equal to the ratio of the TDoA times, and the  $\theta$  azimuth angle:

$$\theta \approx \text{atan2}\left(-\frac{\tau_y}{d_{my}}, -\frac{\tau_x}{d_{mx}}\right) \tag{23}$$

Similarly, in the three-dimensional cartesian space, both the azimuth and elevation angles can be obtained using the four-microphone sensor array shown in Figure 3b. For the sensor array shown in Figure 3b, let the positions of the microphones be  $\mathbf{p}_i = [x_i, y_i, z_i]^T$  and the position of the sound source be  $\mathbf{p}_k = [x_k, y_k, z_k]^T$ . Accordingly, Equations (16) and (17) can be rearranged as follows:

$$\begin{bmatrix} 2(\mathbf{p}_2 - \mathbf{p}_1)^T \\ 2(\mathbf{p}_3 - \mathbf{p}_1)^T \\ 2(\mathbf{p}_4 - \mathbf{p}_1)^T \end{bmatrix} \times [\mathbf{p}_k] = \begin{bmatrix} \mathbf{p}_2^T \mathbf{p}_2 - \mathbf{p}_1^T \mathbf{p}_1 - v_s \tau_{21}(v_s \tau_{21} + 2d_1) \\ \mathbf{p}_3^T \mathbf{p}_3 - \mathbf{p}_1^T \mathbf{p}_1 - v_s \tau_{31}(v_s \tau_{31} + 2d_1) \\ \mathbf{p}_4^T \mathbf{p}_4 - \mathbf{p}_1^T \mathbf{p}_1 - v_s \tau_{41}(v_s \tau_{41} + 2d_1) \end{bmatrix} \tag{24}$$

$$A_2 \mathbf{x}_2 = \mathbf{b}_2 \tag{25}$$

In the new case, the fourth microphone is assumed to be in the z direction and the  $A_2$  and  $\mathbf{b}_2$  matrices are rearranged as follows:

$$A_2 = 2 \times \begin{bmatrix} d_{mx} & 0 & 0 \\ 0 & d_{my} & 0 \\ 0 & 0 & d_{mz} \end{bmatrix} \tag{26}$$

$$\mathbf{b}_2 = \begin{bmatrix} d_{mx}^2 - v_s^2 \times \tau_x^2 - 2v_s \tau_x d_k \\ d_{my}^2 - v_s^2 \times \tau_y^2 - 2v_s \tau_y d_k \\ d_{mz}^2 - v_s^2 \times \tau_z^2 - 2v_s \tau_z d_k \end{bmatrix} \tag{27}$$

After reducing Equation (27) by making similar approximations as in Equation (20), the  $\mathbf{p}_k$  position vector is as follows:

$$\begin{bmatrix} x_k \\ y_k \\ z_k \end{bmatrix} \approx -v_s d_k \begin{bmatrix} \frac{\tau_x}{d_{my}} \\ \frac{d_{mx}}{d_{my}} \\ \frac{\tau_z}{d_{mz}} \end{bmatrix} \tag{28}$$

If we substitute the results found in Equation (28) into Equation (2), the  $\varphi$  elevation angle becomes as follows:

$$\varphi \approx \text{atan2}\left(-\left(\frac{\tau_z}{d_{mz}}\right), \sqrt{\left(\frac{\tau_x}{d_{mx}}\right)^2 + \left(\frac{\tau_y}{d_{my}}\right)^2}\right) \tag{29}$$

In the case where the distances  $d_m$  between the microphones are equal, the Equations (23) and (29) take the following special form:

$$\theta \approx \text{atan2}(-\tau_y, -\tau_x) \tag{30}$$

$$\varphi = \text{atan2}(-\tau_z, \sqrt{\tau_x^2 + \tau_y^2}) \tag{31}$$

The sensor array layouts that satisfy Equations (23) and (29) are shown in Figure 6.

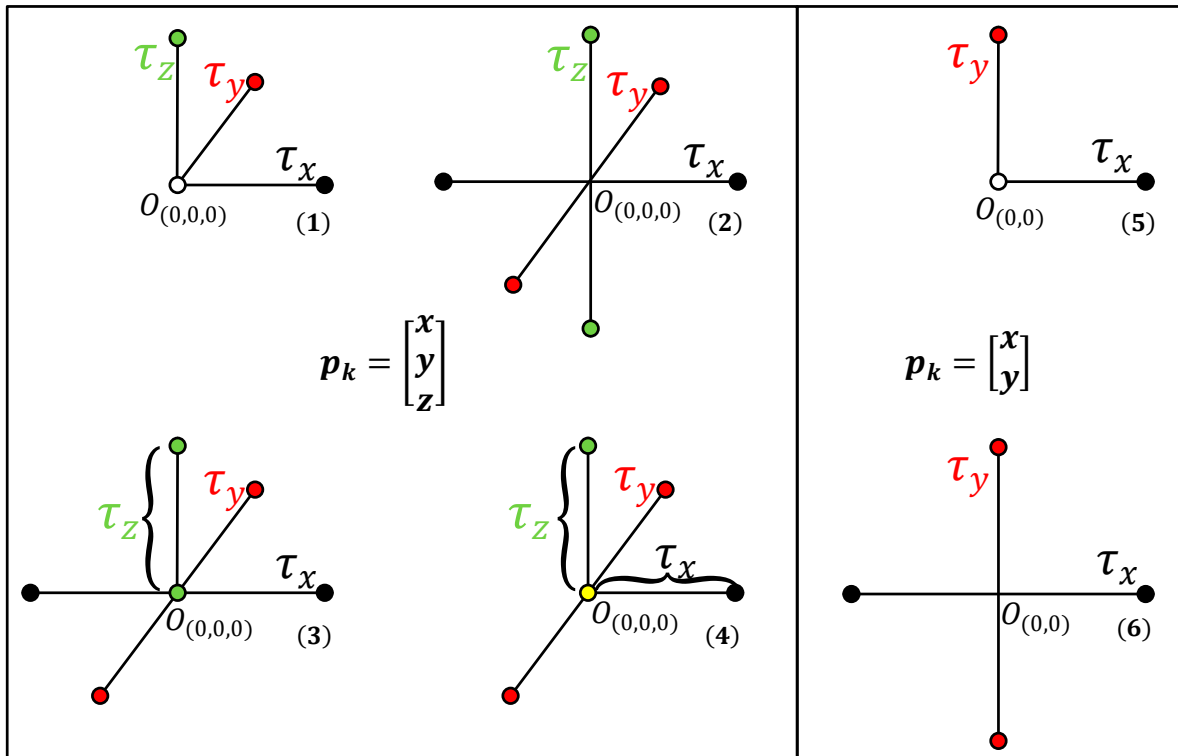


**Figure 6.** Orthogonally located sensor pair microphone arrays (1–4) for azimuth and elevation angles, (5,6) for only azimuth angle.

### 3.2. Simulations

The first simulation studies were performed in two-dimensional space using the fifth microphone array shown in Figure 6. In real-time applications, when measuring the TDoA time, hardware time errors of  $\Delta t < t_s$ , depending on the sampling frequency of the audio recording devices, and  $N_{err}$  measurement sample errors caused by environmental noise as a result of the GCC-Phat algorithm are introduced. These errors are modeled in our simulation study as shown in Figure 4.

The simulation studies in the XY plane assumed that the distance of the sound source is 100 m. The largest measurement errors in the direction of arrival are at angles below  $10^\circ$  [29]. Figure 7 shows the results obtained using different  $d_m$  distances in the case of  $d_k = 100$  m and  $F_s = 44.1$  kHz.

Figure 8 shows the effect of the source position on the direction-of-arrival estimation for near and far distances. The results for the source at 20 m and 500 m distances are shown when the sampling frequency and the microphone spacing are fixed.

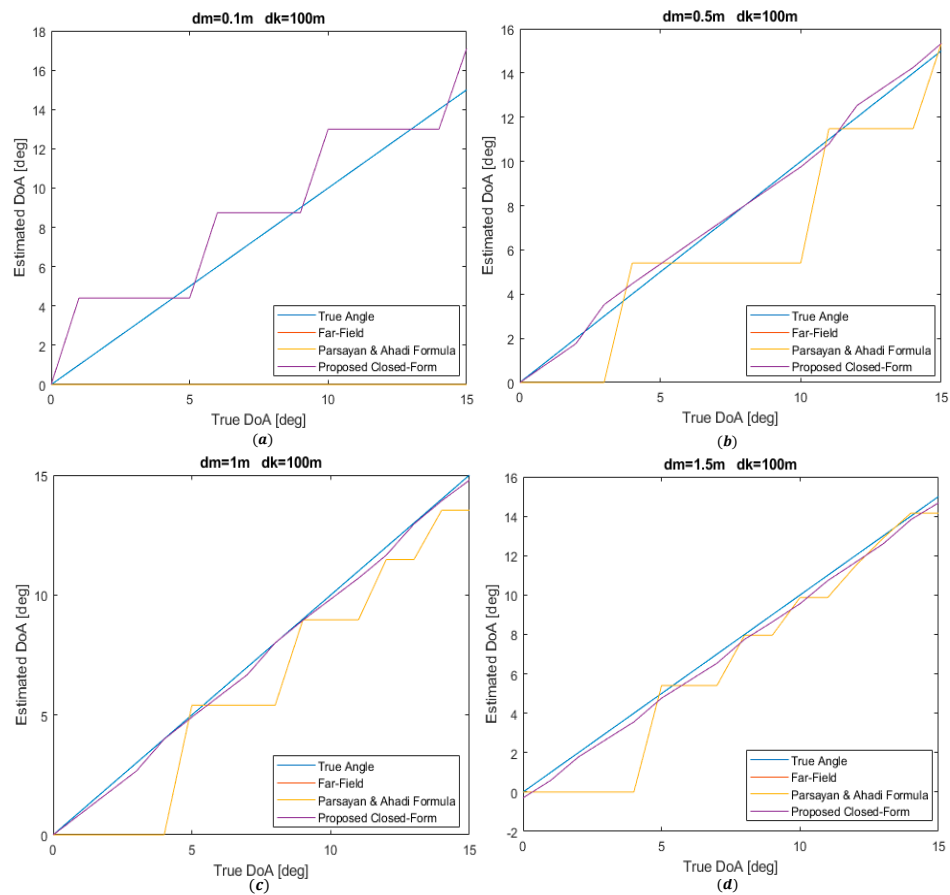


**Figure 7.** The effect of the distance between microphone pairs on the direction-of-arrival estimation in the case of  $d_k = 100$  m and  $F_s = 44.1$  kHz (a)  $d_m = 0.1$  m, (b)  $d_m = 0.5$  m, (c)  $d_m = 1$  m, and (d)  $d_m = 1.5$  m.

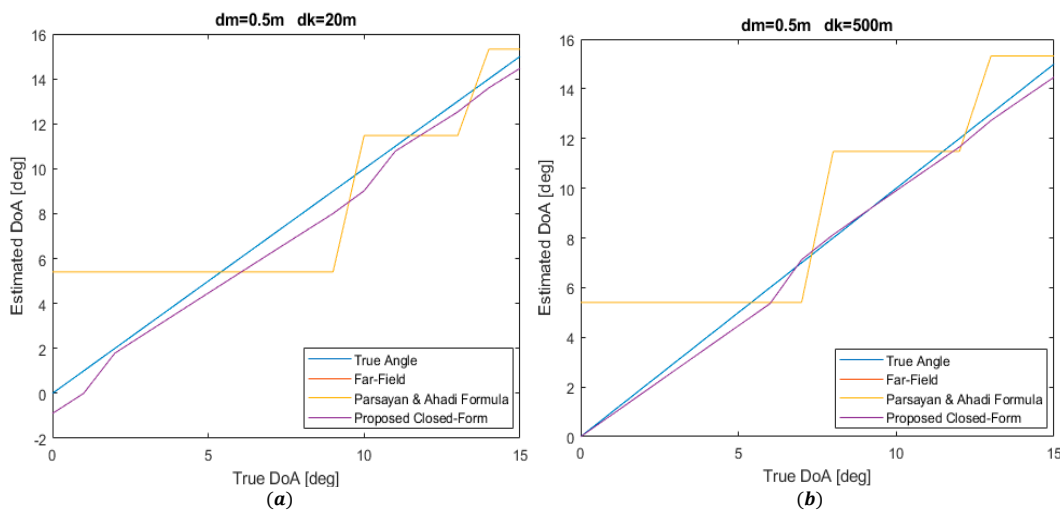


**Figure 8.** The effect of the source distance on the direction-of-arrival estimation in the case of  $d_m = 0.5$  m and  $F_s = 44.1$  kHz (a)  $d_k = 20$  m and (b)  $d_k = 500$  m.

The error changes of the estimates made with 1 degree increments between 0 and 90 degrees while the  $d_k$  distance increases from 5 m to 100 m with 1 m increments, and the

$d_m$  distance increases from 0.1 m to 1 m with 0.1 m increments are shown in Figure 9. The error values are calculated using the mean absolute error function:

$$MAE = \frac{1}{N} \sum_0^N |\theta - \hat{\theta}| \tag{32}$$

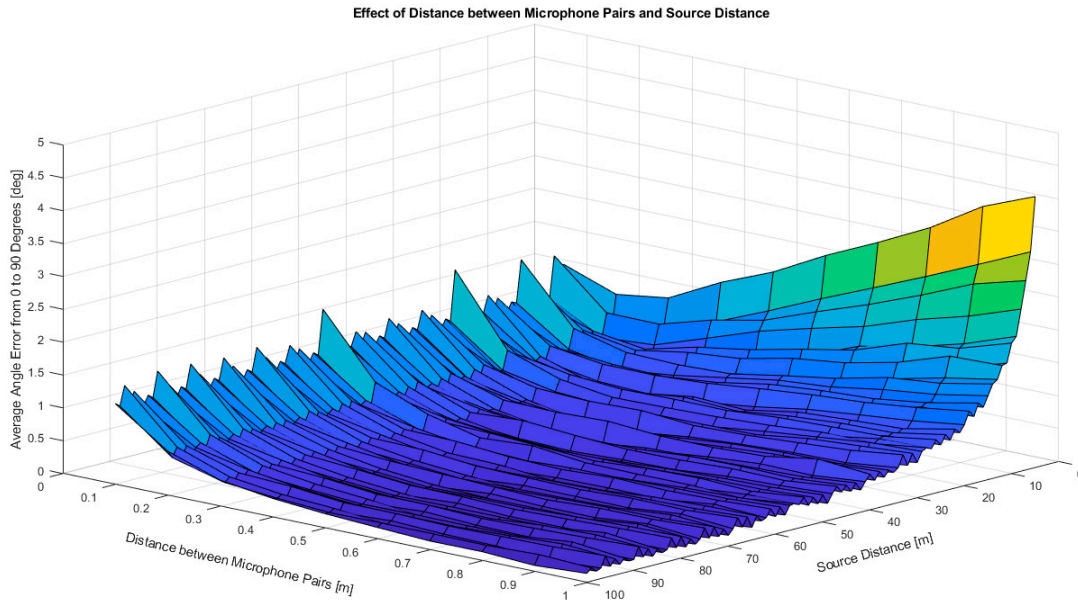
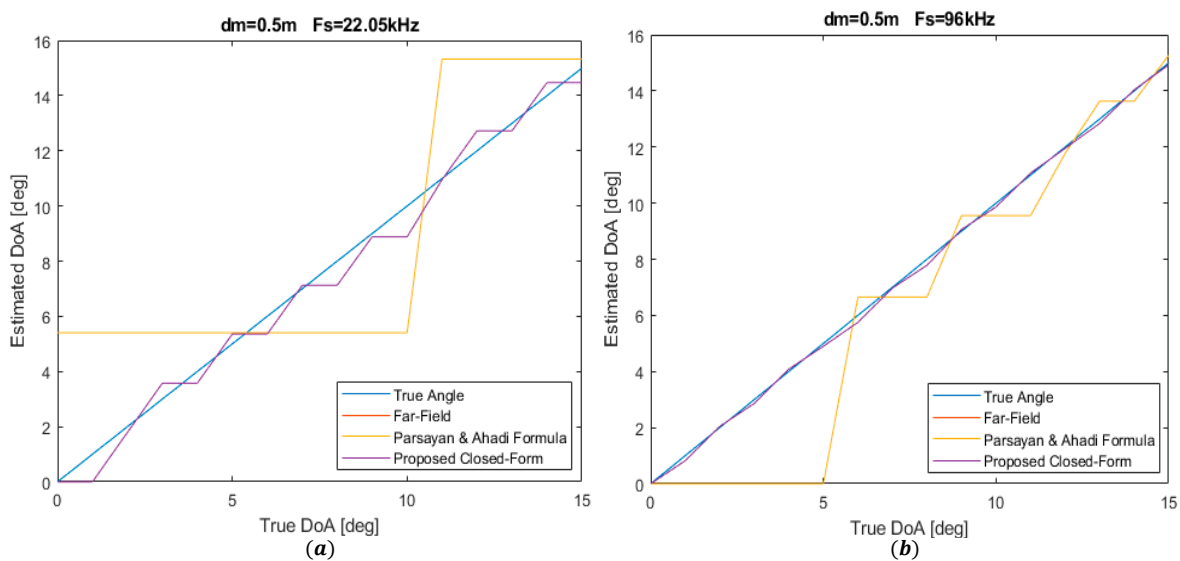


**Figure 9.** The change in the absolute average error between 0 and 90 degrees in the case of  $d_m \in [0.1, 1]$  m,  $d_k \in [5, 100]$  m  $F_s = 44.1$  kHz.

The expressions  $\theta$  and  $\hat{\theta}$  represent the true and measured angle values, respectively.

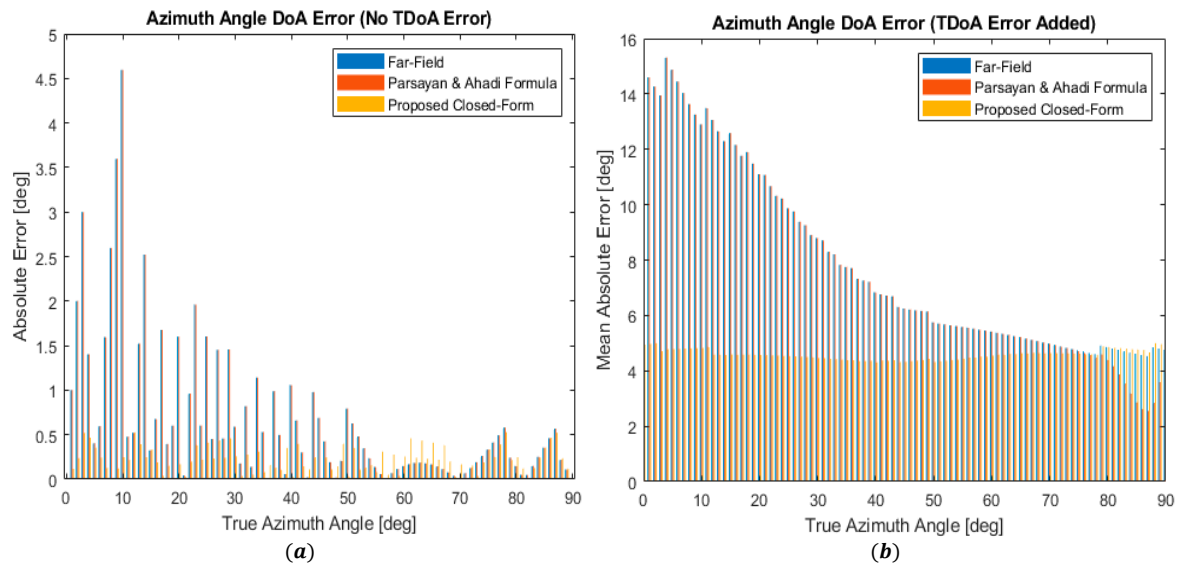
The mean error decreases below  $0.5^\circ$  after  $d_m > 0.3$  m and  $d_k > 35$  m. Additionally, the maximum error values are reached as the  $d_m/d_k$  ratio approaches one.

The results obtained for different sampling frequencies with fixed microphone spacing and source position are shown in Figure 10.



**Figure 10.** The effect of sampling frequency on the elevation angle estimation in the case of  $d_m = 0.5$  m,  $d_k = 100$  m (a)  $F_s = 22.05$  kHz and (b)  $F_s = 96$  kHz.

The simulation studies that led to the results in Figures 7–10 were investigated under the assumption that the GCC-Phat error in the model shown in Figure 4 is zero. In real-time applications, errors occur in the measurement of TDoA values due to environmental noises, reverberation, and differences in microphone detection patterns. Normally distributed noise with  $N_{err} = N(0, 3)$  was added instead of these errors, and the mean absolute error values were obtained by simulation with 1000 repetitions. The simulation results without the added error are shown in Figure 11a, and the simulation results with the added error are shown in Figure 11b.



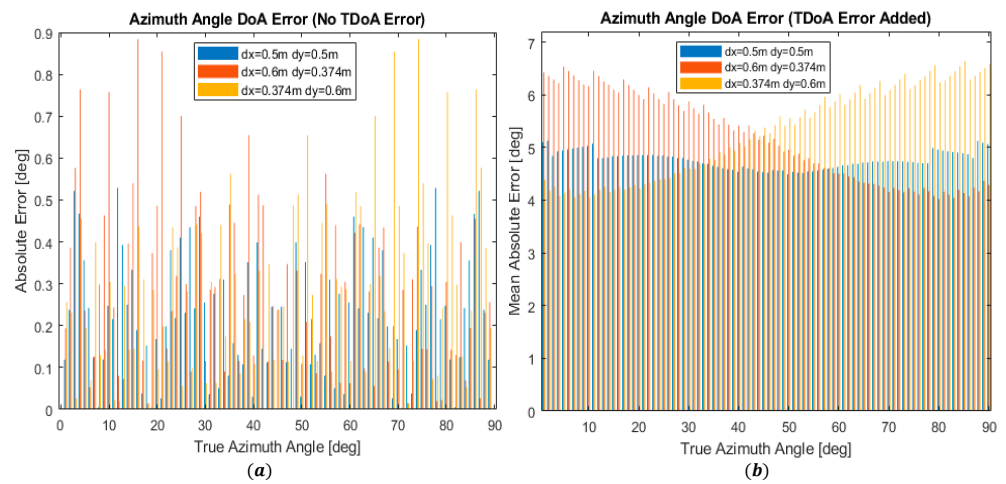
**Figure 11.** The azimuth angle estimation errors between 0 and 90 degrees in the case of  $d_m = 0.5$  m,  $d_k = 100$  m  $F_s = 44.1$  kHz—(a) without error addition and (b) with error addition.

Figure 11a shows that our proposed method produces better results than other methods except for the 55–70-degree range. Figure 11b shows that our proposed method produces stable results than other methods up to 80 degrees. Parsayan and Ahadi’s method is more successful in the 79–89-degree range. Table 1 shows the total average error values of the methods in the 0–90-degree range.

**Table 1.** The average values of the azimuth angle estimation errors between 0 and 90 degrees in the case of  $d_m = 0.5$  m,  $d_k = 100$  m  $F_s = 44.1$  kHz.

| Error Edit | Far Field | Parsayan and Ahadi | Proposed Closed Form |
|------------|-----------|--------------------|----------------------|
| No         | 0.65      | 0.65               | 0.22                 |
| $N(0, 3)$  | 8.01      | 7.85               | 4.72                 |

To investigate the change in the estimation error when the distance between the pairs of microphones placed perpendicularly is not equal, three different microphone array geometries were created with  $d_{mx} = 0.5 - d_{my} = 0.5$ ,  $d_{mx} = 0.6 - d_{my} = 0.374$ , and  $d_{mx} = 0.374 - d_{my} = 0.6$ , ensuring that the hypotenuses of the triangles formed by the microphones have equal lengths. The simulation results without error are shown in Figure 12a, and with noise are shown in Figure 12b.



**Figure 12.** The effect of unequal microphone spacing on the azimuth angle estimation—(a) without error addition and (b) with error addition.

Although no clear difference can be seen in Figure 12a, it can be seen in Figure 12b that the three changing conditions are more successful in the 0–30-degree range and that two of them are more successful in the 60–90-degree range. Table 2 shows the total average error values of the three different conditions in the 0–90-degree range.

**Table 2.** Average values of estimation errors between 0 and 90 degrees for different microphone array geometries.

| Error Edit | $d_x = 0.5 \ d_y = 0.5$ | $d_x = 0.6 \ d_y = 0.374$ | $d_x = 0.374 \ d_y = 0.6$ |
|------------|-------------------------|---------------------------|---------------------------|
| No         | 0.2197                  | 0.2776                    | 0.2776                    |
| $N(0, 3)$  | 4.7423                  | 5.2387                    | 5.2351                    |

The performance of the elevation angle estimation calculated by Equation (31) was investigated by simulation studies using the first microphone array in Figure 6. The results obtained without adding error, assuming  $d_m = 0.5 \text{ m}$ ,  $d_k = 100 \text{ m}$ ,  $F_s = 44.1 \text{ kHz}$ , and azimuth angle  $\theta = 45$  are shown in Figure 13a, and obtained by adding noise are shown in Figure 13b.

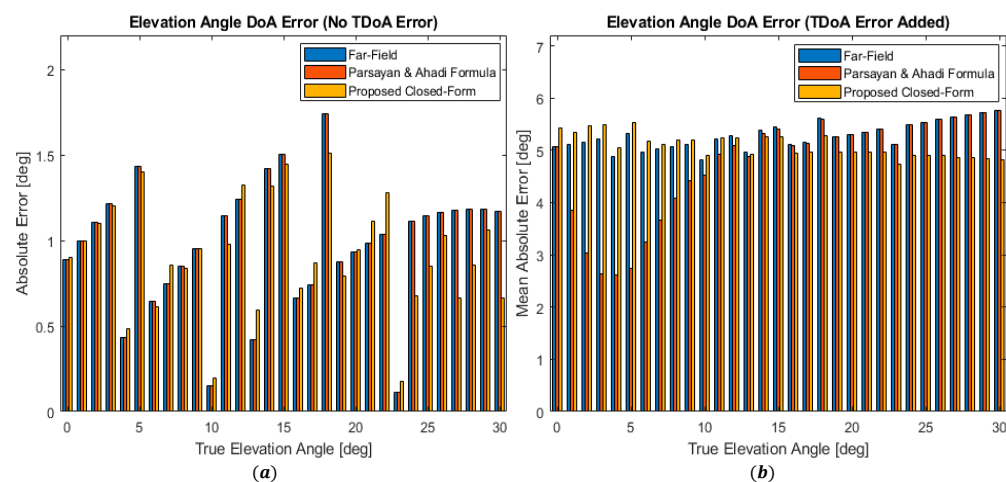


**Figure 13.** The elevation angle estimation errors between 0 and 30 degrees in the case of  $d_m = 0.5 \text{ m}$ ,  $d_k = 100 \text{ m}$ ,  $F_s = 44.1 \text{ kHz}$ , and  $\theta = 45$ —(a) without error addition and (b) with error addition.

The average error values of the error graphs shown in Figure 13 are presented in Table 3.

**Table 3.** Average error values of elevation angle estimation between 0 and 30 degrees in the case of  $d_m = 0.5$  m,  $d_k = 100$  m,  $F_s = 44.1$  kHz,  $\theta = 45$ .

| Error Edit | Far Field | Parsayan and Ahadi | Proposed Closed Form |
|------------|-----------|--------------------|----------------------|
| No         | 0.98      | 0.98               | 0.92                 |
| $N(0,3)$   | 5.33      | 4.75               | 5.04                 |

The far-field approach cannot produce a solution when the expression to be taken the inverse of, especially at right angles, exceeds the range of  $-1 \leq \cos^{-1}\left(\frac{v_s \times \tau}{d_m}\right) \leq 1$  due to measurement errors in the TDoA value. This significantly impairs the measurement sensitivity at right angles. The solution in the far-field approach is also dependent on the speed of sound. The speed of sound varies depending on the weather conditions and affects the measurement results. Additionally, in the far-field approach, the number of samples obtained by the GCC-Phat algorithm is multiplied by  $t_s$  time and added to the formula. This increases the number of mathematical and algorithmic operations. Our proposed arrival angle detection method, since it is obtained from the source position equation, the quadrant in which the arrival angle is located, is precisely determined by the *arctan*2 function. Studies have been performed to determine the azimuth and elevation angles with the *tan* function, but the quadrant information is still obtained by the algorithm [21–23]. Our proposed method is obtained as the result of a single function, not as a function of conditions like other methods. Additionally, in the solutions obtained with the tangent function, in the regions where the cosine angle will be close to zero, indeterminateness occurs due to measurement errors in the TDoA values.

Our proposed method uses the sample differences directly obtained from the GCC-Phat algorithm. Therefore, it produces  $v_s$  independent results. The *arctan*2 function does not create indeterminateness when the *cos* value is zero. Our proposed method is faster and produces more stable results, especially against measurement errors.

#### 4. Experimental Results

Muzzle blast DoA detection is a widely used application in outdoor environments. In our experimental study, we determined the direction of arrival of generated explosion sounds. To achieve this, we created an experimental field as shown in Figure 14a. Each point in the experimental field was marked with a Topcon GR-5 GNSS device with an accuracy of  $\pm 2$  cm. At the zero point of our experimental site, the microphone assembly designed in the geometry shown in Figure 6 (2) and in Figure 14b was placed with its origin 190 cm above the ground. Low-noise, high-sensitivity EM272 condenser electret omnidirectional microphones were used to capture explosion sounds at long distances. The distance between microphones on the same axis was set to 1 m. The ZOOM H8 sound recorder was used to record six microphones synchronously. Explosions were recorded at 10 different distances from 50 m to 500 m in 50 m increments and at angles of 0,  $-5$ ,  $-10$ ,  $-15$ ,  $-30$ ,  $-45$ ,  $-60$ ,  $-75$ , and  $-90$ .



**Figure 14.** (a) Experiment site for explosion sound recording (b) microphone array and axes used.

To keep the environmental conditions constant, the microphone array was rotated at the desired angles. In this way, 90 separate locations were created and two explosions were created from each location, for a total of 180 explosions. The explosion sounds were generated using a sound gun at a height of 1.5 m from the ground.

The TDoA times between microphones for each explosion and  $\hat{\theta}$  the angles calculated from these values using the GCC-Phat algorithm are given in Table 4 and Table 7. The  $\tau_x$ ,  $\tau_y$ , and  $\tau_z$  values are expressed in units of sample. In our experiment, one sample time is equal to 22.68  $\mu$ s. The azimuth angle is calculated by Equation (30) according to the values in Table 4 and the unit of azimuth angle is degrees.

**Table 4.** Experimental TDoA values and calculated DoA obtained in explosions at different angles and distances.

| $\theta$ | Shot No | TDoA/ $\hat{\theta}$ | 50 m   | 100 m  | 150 m  | 200 m | 250 m  | 300 m  | 350 m  | 400 m | 450 m  | 500 m |
|----------|---------|----------------------|--------|--------|--------|-------|--------|--------|--------|-------|--------|-------|
| 0°       | 1       | $\tau_x$             | -128   | -129   | -134   | -134  | -135   | -134   | -133   | -135  | -134   | -131  |
|          |         | $\tau_y$             | 2      | 5      | -1     | -1    | 0      | -5     | 0      | -1    | 0      | 0     |
|          |         | $\hat{\theta}$       | -0.89  | -2.22  | 0.43   | 0.43  | 0      | 2.14   | 0      | 0.42  | 0      | 0     |
|          | 2       | $\tau_x$             | 128    | 133    | 128    | 134   | 135    | 135    | 134    | 134   | 134    | 133   |
|          |         | $\tau_y$             | -1     | 2      | 3      | 1     | 2      | 0      | 0      | -1    | 0      | 0     |
|          |         | $\hat{\theta}$       | -0.45  | 0.86   | 1.34   | 0.43  | 0.85   | 0      | 0      | -0.43 | 0      | 0     |
| -5°      | 1       | $\tau_x$             | 127    | 130    | 129    | 129   | 129    | 130    | 129    | 128   | 129    | 129   |
|          |         | $\tau_y$             | -7     | -12    | -13    | -18   | -13    | -14    | -13    | -13   | -12    | -9    |
|          |         | $\hat{\theta}$       | -3.16  | -5.27  | -5.76  | -7.94 | -5.76  | -6.15  | -5.76  | -5.80 | -5.32  | -4.00 |
|          | 2       | $\tau_x$             | 127    | 129    | 129    | 129   | 128    | 129    | 130    | 129   | 129    | 130   |
|          |         | $\tau_y$             | -5     | -13    | -12    | -14   | -15    | -15    | -10    | -12   | -9     | -6    |
|          |         | $\hat{\theta}$       | -2.26  | -5.76  | -5.32  | -6.19 | -6.68  | -6.63  | -4.40  | -5.32 | -3.99  | -2.64 |
| -10°     | 1       | $\tau_x$             | 126    | 125    | 126    | 128   | 128    | 127    | 127    | 127   | 126    | 126   |
|          |         | $\tau_y$             | -25    | -23    | -23    | -18   | -22    | -26    | -20    | -20   | -24    | -20   |
|          |         | $\hat{\theta}$       | -11.22 | -10.43 | -10.35 | -8.01 | -9.75  | -11.57 | -8.95  | -8.95 | -10.78 | -9.02 |
|          | 2       | $\tau_x$             | 126    | 127    | 127    | 127   | 128    | 128    | 127    | 127   | 127    | 126   |
|          |         | $\tau_y$             | -21    | -22    | -23    | -18   | -24    | -24    | -23    | -15   | -21    | -21   |
|          |         | $\hat{\theta}$       | -9.46  | -9.83  | -10.27 | -8.07 | -10.62 | -10.62 | -10.27 | -6.74 | -9.32  | -9.46 |

**Table 4.** *Cont.*

| $\theta$ | Shot No | TDoA/ $\hat{\theta}$ | 50 m   | 100 m  | 150 m  | 200 m  | 250 m  | 300 m  | 350 m  | 400 m  | 450 m  | 500 m  |        |
|----------|---------|----------------------|--------|--------|--------|--------|--------|--------|--------|--------|--------|--------|--------|
| -15°     | 1       | $\tau_x$             | 128    | 125    | 125    | 125    | 125    | 125    | 125    | 125    | 123    | 122    | 126    |
|          |         | $\tau_y$             | -31    | -32    | -34    | -32    | -33    | -31    | -33    | -30    | -30    | -35    | -29    |
|          |         | $\hat{\theta}$       | -13.61 | -14.36 | -15.22 | -14.36 | -14.79 | -13.93 | -14.79 | -13.71 | -13.71 | -16.01 | -12.96 |
|          | 2       | $\tau_x$             | 126    | 124    | 124    | 126    | 125    | 125    | 126    | 126    | 124    | 126    | 124    |
|          |         | $\tau_y$             | -31    | -31    | -34    | -33    | -32    | -33    | -31    | -31    | -34    | -34    | -29    |
|          |         | $\hat{\theta}$       | -13.82 | -14.04 | -15.33 | -14.68 | -14.36 | -14.79 | -13.82 | -13.82 | -15.33 | -15.10 | -13.16 |
| -30°     | 1       | $\tau_x$             | 111    | 113    | 115    | 112    | 113    | 111    | 115    | 113    | 115    | 115    | 114    |
|          |         | $\tau_y$             | -62    | -65    | -60    | -65    | -61    | -68    | -62    | -62    | -62    | -64    | -61    |
|          |         | $\hat{\theta}$       | -29.19 | -29.91 | -27.55 | -30.13 | -28.36 | -31.49 | -28.33 | -28.75 | -28.75 | -29.10 | -28.15 |
|          | 2       | $\tau_x$             | 113    | 111    | 115    | 113    | 113    | 112    | 112    | 113    | 113    | 113    | 111    |
|          |         | $\tau_y$             | -61    | -66    | -60    | -63    | -63    | -64    | -65    | -62    | -62    | -60    | -66    |
|          |         | $\hat{\theta}$       | -28.36 | -30.74 | -27.55 | -29.14 | -29.14 | -29.75 | -30.13 | -28.75 | -28.75 | -27.97 | -30.74 |
| -45°     | 1       | $\tau_x$             | 91     | 89     | 90     | 91     | 90     | 90     | 94     | 89     | 90     | 90     | 89     |
|          |         | $\tau_y$             | -94    | -96    | -93    | -91    | -93    | -93    | -88    | -93    | -93    | -92    | -94    |
|          |         | $\hat{\theta}$       | -45.93 | -47.17 | -45.94 | -45    | -45.94 | -45.94 | -43.11 | -46.26 | -46.26 | -45.63 | -46.57 |
|          | 2       | $\tau_x$             | 92     | 92     | 91     | 93     | 91     | 89     | 92     | 91     | 91     | 89     | 85     |
|          |         | $\tau_y$             | -95    | -92    | -92    | -90    | -92    | -94    | -89    | -92    | -92    | -94    | -96    |
|          |         | $\hat{\theta}$       | -45.92 | -45    | -45.31 | -44.06 | -45.31 | -46.57 | -44.05 | -45.31 | -45.31 | -46.57 | -48.48 |
| -60°     | 1       | $\tau_x$             | 65     | 64     | 67     | 60     | 68     | 61     | 65     | 64     | 60     | 60     | 66     |
|          |         | $\tau_y$             | -112   | -114   | -112   | -116   | -111   | -115   | -113   | -113   | -113   | -116   | -112   |
|          |         | $\hat{\theta}$       | -59.87 | -60.69 | -59.11 | -62.65 | -58.51 | -62.06 | -60.09 | -60.47 | -60.47 | -62.65 | -59.49 |
|          | 2       | $\tau_x$             | 65     | 65     | 66     | 66     | 68     | 61     | 68     | 64     | 63     | 63     | 69     |
|          |         | $\tau_y$             | -109   | -113   | -113   | -113   | -112   | -114   | -112   | -114   | -114   | -115   | -111   |
|          |         | $\hat{\theta}$       | -59.19 | -60.09 | -59.71 | -59.71 | -58.74 | -61.85 | -58.74 | -60.69 | -60.69 | -61.29 | -58.13 |
| -75°     | 1       | $\tau_x$             | 34     | 33     | 32     | 27     | 30     | 38     | 37     | 32     | 36     | 33     |        |
|          |         | $\tau_y$             | -128   | -127   | -127   | -129   | -128   | -125   | -125   | -127   | -127   | -125   | -126   |
|          |         | $\hat{\theta}$       | -75.12 | -75.43 | -75.86 | -78.18 | -76.81 | -73.09 | -73.51 | -75.86 | -75.86 | -73.93 | -75.32 |
|          | 2       | $\tau_x$             | 32     | 34     | 29     | 30     | 31     | 34     | 37     | 34     | 34     | 35     | 36     |
|          |         | $\tau_y$             | -129   | -126   | -128   | -128   | -127   | -126   | -126   | -127   | -127   | -124   | -126   |
|          |         | $\hat{\theta}$       | -76.07 | -74.90 | -77.23 | -76.81 | -76.28 | -74.90 | -73.64 | -75.01 | -75.01 | -74.24 | -74.06 |
| -90°     | 1       | $\tau_x$             | -2     | -4     | -7     | -4     | 0.01   | -6     | -5     | -4     | -2     | -7     |        |
|          |         | $\tau_y$             | -131   | -132   | -132   | -134   | -135   | -131   | -133   | -131   | -131   | -131   |        |
|          |         | $\hat{\theta}$       | -90.88 | -91.74 | -93.04 | -91.71 | -90.00 | -92.62 | -92.15 | -91.75 | -91.75 | -90.88 |        |
|          | 2       | $\tau_x$             | -2     | -2     | -4     | -1     | 0.01   | -6     | -6     | -4     | -4     | -4     |        |
|          |         | $\tau_y$             | -130   | -132   | -132   | -134   | -135   | -131   | -132   | -135   | -135   | -131   |        |
|          |         | $\hat{\theta}$       | -90.88 | -90.87 | -91.74 | -90.43 | -90.00 | -92.62 | -92.60 | -91.70 | -91.70 | -91.75 |        |

The average error values of the angle values obtained experimentally and calculated with Equation (32) are given in Table 5, and the error graph is shown in Figure 15. When Table 4 is examined, no clear separation is seen in the amount of error according to the angle values.

**Table 5.** MAE values of experimental azimuth angle results with respect to explosion angle.

| Angle | 0°   | -5°  | -10° | -15° | -30° | -45° | -60° | -75° | -90° |
|-------|------|------|------|------|------|------|------|------|------|
| Shot1 | 0.65 | 1.06 | 0.97 | 0.87 | 1.23 | 1.13 | 1.16 | 1.21 | 1.78 |
| Shot2 | 0.44 | 1.26 | 0.89 | 0.71 | 1.10 | 1.04 | 0.97 | 0.97 | 1.30 |
| Mean  | 0.55 | 1.16 | 0.93 | 0.79 | 1.16 | 1.08 | 1.07 | 1.09 | 1.54 |

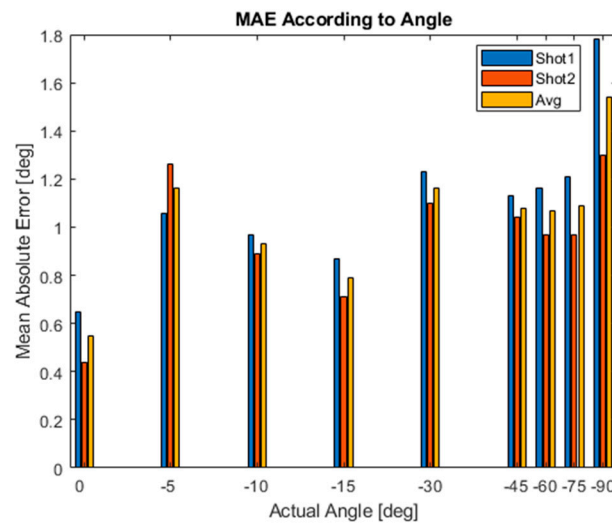


**Figure 15.** MAE values of the azimuth angle values calculated with experimental results with respect to explosion angle.

To investigate the change of the errors with distance, the average of the errors of the shots made at different angles from the same distance was taken to create Table 6. The error change graph with distance according to the values in Table 6 is shown in Figure 16. When Figure 16 is examined, no clear separation is seen in the values of the errors with distance.

**Table 6.** MAE values of experimental azimuth results with respect to explosion distance.

| Distance | 50 m | 100 m | 150 m | 200 m | 250 m | 300 m | 350 m | 400 m | 450 m | 500 m |
|----------|------|-------|-------|-------|-------|-------|-------|-------|-------|-------|
| Shot1    | 0.91 | 0.97  | 1.10  | 1.52  | 0.79  | 1.66  | 1.04  | 1.02  | 0.92  | 1.26  |
| Shot2    | 1.14 | 0.51  | 1.03  | 0.91  | 0.83  | 0.98  | 0.93  | 0.92  | 1.02  | 1.36  |
| Mean     | 1.02 | 0.74  | 1.07  | 1.22  | 0.81  | 1.32  | 0.98  | 0.97  | 0.97  | 1.31  |

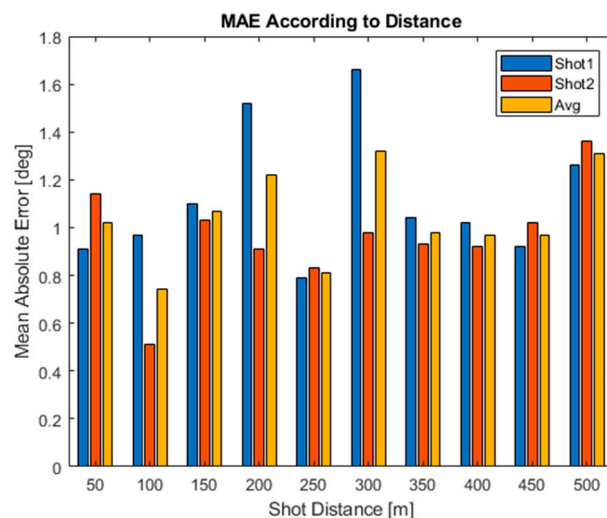


**Figure 16.** MAE values of the azimuth angle values calculated with experimental results with respect to explosion distance.

As seen in Figure 14b, the test site had a slight slope with a maximum elevation angle of  $\varphi_{max} = -1.24^\circ$  at 50 m and a minimum elevation angle of  $\varphi_{min} = -0.82^\circ$  at 500 m. The  $\hat{\varphi}$  angles calculated using Equation (31) are presented in degrees in Table 7. The experimental  $\tau_z$  values are expressed in units of sample.

**Table 7.** Experimental TDoA values and calculated elevation angle obtained in explosions at different angles and distances.

| Azimuth Angle | Shot No | TDoA/ $\hat{\phi}$ | 50 m  | 100 m | 150 m | 200 m | 250 m | 300 m | 350 m | 400 m | 450 m | 500 m |
|---------------|---------|--------------------|-------|-------|-------|-------|-------|-------|-------|-------|-------|-------|
| 0°            | 1       | $\tau_z$           | -3    | -6    | -5    | 0     | 0     | -1    | 0     | 0     | 0     | 0     |
|               |         | $\hat{\phi}$       | -1.34 | -2.66 | -2.14 | 0     | 0     | -0.43 | 0     | 0     | 0     | 0     |
| 0°            | 2       | $\tau_z$           | -6    | -5    | -1    | 0     | 0     | -1    | -1    | -1    | 0     | 0     |
|               |         | $\hat{\phi}$       | -2.68 | -2.15 | -0.45 | 0     | 0     | -0.42 | -0.43 | -0.43 | 0     | 0     |
| -5°           | 1       | $\tau_z$           | -10   | -7    | -4    | 0     | -1    | 3     | 0     | 0     | 1     | 2     |
|               |         | $\hat{\phi}$       | -4.50 | -3.07 | -1.77 | 0     | -0.44 | 1.31  | 0     | 0     | 0.44  | 0.89  |
| -5°           | 2       | $\tau_z$           | -8    | -5    | -4    | 2     | 2     | 2     | 0     | -2    | -3    | -3    |
|               |         | $\hat{\phi}$       | -3.60 | -2.21 | -1.77 | 0.88  | 0.89  | 0.88  | 0     | -0.88 | -1.33 | -1.32 |
| -10°          | 1       | $\tau_z$           | -2    | -2    | -1    | 0     | -1    | 3     | 2     | -2    | -4    | 4     |
|               |         | $\hat{\phi}$       | -0.89 | -0.90 | -0.45 | 0     | -0.44 | 1.33  | 0.89  | -0.89 | -1.77 | 1.80  |
| -10°          | 2       | $\tau_z$           | -4    | -3    | 0     | -3    | 4     | 4     | 2     | 2     | 0     | 2     |
|               |         | $\hat{\phi}$       | -1.79 | -1.33 | 0     | -1.34 | 1.76  | 1.76  | 0.89  | 0.90  | 0     | 0.90  |
| -15°          | 1       | $\tau_z$           | -1    | -4    | -3    | 1     | 1     | -2    | 3     | 5     | 1     | -1    |
|               |         | $\hat{\phi}$       | -0.44 | -1.78 | -1.33 | 0.44  | 0.44  | -0.89 | 1.33  | 2.26  | 0.45  | -0.44 |
| -15°          | 2       | $\tau_z$           | 3     | -3    | -4    | 1     | 3     | -3    | 3     | 4     | 0     | 0     |
|               |         | $\hat{\phi}$       | 1.32  | -1.35 | -1.78 | 0.44  | 1.33  | -1.33 | 1.33  | 1.78  | 0     | 0     |
| -30°          | 1       | $\tau_z$           | -6    | -4    | -1    | -1    | 3     | -2    | 5     | 0     | 0     | -1    |
|               |         | $\hat{\phi}$       | -2.70 | -1.76 | -0.44 | -0.44 | 1.34  | -0.88 | 2.19  | 0     | 0     | -0.44 |
| -30°          | 2       | $\tau_z$           | -6    | -6    | 2     | -2    | -3    | -5    | 9     | -2    | -1    | -2    |
|               |         | $\hat{\phi}$       | -2.68 | -2.66 | 0.88  | -0.89 | -1.33 | -2.22 | 3.98  | -0.89 | -0.45 | -0.89 |
| -45°          | 1       | $\tau_z$           | -8    | -8    | -2    | 1     | 1     | 0     | 2     | 3     | -1    | 0     |
|               |         | $\hat{\phi}$       | -3.50 | -3.50 | -0.89 | 0.45  | 0.44  | 0     | 0.89  | 1.34  | -0.45 | 0     |
| -45°          | 2       | $\tau_z$           | -9    | -6    | -1    | 0     | -1    | -3    | 1     | 6     | -2    | 2     |
|               |         | $\hat{\phi}$       | -3.89 | -2.64 | -0.44 | 0     | -0.44 | -1.33 | 0.48  | 2.66  | -0.89 | 0.89  |
| -60°          | 1       | $\tau_z$           | -4    | -5    | -3    | 0     | -3    | -2    | -1    | 2     | 1     | -1    |
|               |         | $\hat{\phi}$       | -1.77 | -2.19 | -1.32 | 0     | -1.32 | -0.88 | -0.44 | 0.88  | 0.44  | -0.44 |
| -60°          | 2       | $\tau_z$           | -8    | -4    | -5    | -1    | -1    | 4     | -1    | 1     | 2     | 0     |
|               |         | $\hat{\phi}$       | -3.61 | -1.76 | -2.19 | -0.44 | -0.44 | 1.77  | -0.44 | 0.44  | 0.87  | 0     |
| -75°          | 1       | $\tau_z$           | -2    | -3    | -4    | -7    | -2    | -3    | 2     | -2    | 4     | 0     |
|               |         | $\hat{\phi}$       | -0.87 | -1.31 | -1.75 | -3.04 | -0.87 | -1.32 | 0.88  | -0.88 | 1.76  | 0     |
| -75°          | 2       | $\tau_z$           | -3    | -4    | -5    | -4    | -1    | -2    | -1    | -6    | 0     | 5     |
|               |         | $\hat{\phi}$       | -1.29 | -1.76 | -2.18 | -1.74 | -0.44 | -0.88 | -0.44 | -2.61 | 0     | 2.19  |
| -90°          | 1       | $\tau_z$           | -3    | -4    | -3    | -1    | -1    | -1    | -2    | 2     | 1     | 0     |
|               |         | $\hat{\phi}$       | -1.31 | -1.74 | -1.30 | -0.43 | -0.42 | -0.44 | -0.86 | 0.87  | 0.44  | 0     |
| -90°          | 2       | $\tau_z$           | -9    | -2    | -4    | 0     | 1     | -3    | -2    | 0     | -1    | 4     |
|               |         | $\hat{\phi}$       | -3.96 | -0.87 | -1.74 | 0     | 0.42  | -1.31 | -0.87 | 0     | -0.44 | 1.76  |

The MAE error graph for each distance value for the results obtained in Table 7 is shown in Figure 17. The maximum values in the Figure 17 graph are given in Table 8. The maximum elevation angle at 50 m was also obtained in the experimental study. After 150 m, similar results were obtained.

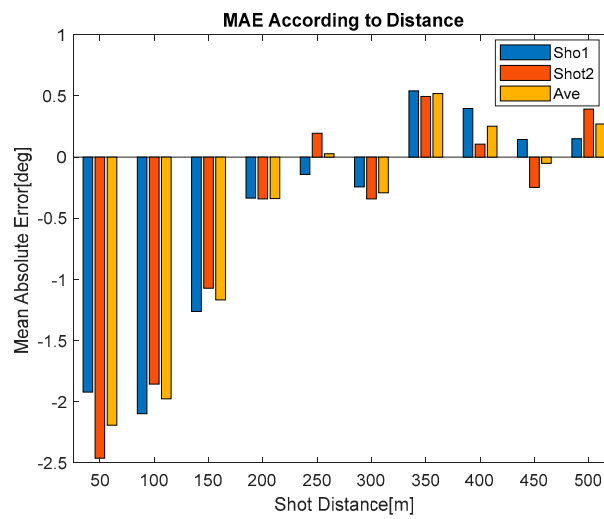


**Figure 17.** MAE values of the elevation angle values calculated with experimental results with respect to explosion distance.

**Table 8.** MAE values of experimental elevation angle results with respect to explosion distance.

| Distance | 50 m  | 100 m | 150 m | 200 m | 250 m | 300 m | 350 m | 400 m | 450 m | 500 m |
|----------|-------|-------|-------|-------|-------|-------|-------|-------|-------|-------|
| Shot1    | -1.92 | -2.1  | -1.26 | -0.34 | -0.14 | -0.24 | 0.54  | 0.40  | 0.14  | 0.15  |
| Shot2    | -2.47 | -1.86 | -1.07 | -0.34 | 0.19  | -0.34 | 0.50  | 0.11  | -0.25 | 0.39  |
| Mean     | -2.19 | -1.98 | -1.17 | -0.34 | 0.03  | -0.29 | 0.52  | 0.25  | -0.05 | 0.27  |

### 5. Discussion

By analyzing Figures 7–10, it can be seen that the far-field solution and the solution proposed in [29] give close results. According to the appropriate microphone aperture and source distance, the angle error value decreases below  $0.5^\circ$  with our proposed method. In Figure 7c, at 44.1 kHz sampling frequency, 0.5 m distance between microphones, and 100 m the sound source distance, the far-field solution and other methods produce an angular error of up to  $3^\circ$ . In the same case, our proposed method produces an angular error of less than  $0.5^\circ$ . By analyzing the result of Figure 11, while a significant degree measurement error occurs between 0–30 degrees in the far-field approach and proposed [29], our proposed method has the same stability at all angle values.

When Figures 7b and 8b are analyzed together, it can be seen that for very close and very far source distances, the angle errors increase for both existing methods. In our proposed solution, there is no significant change in the angle errors, which shows that it produces more stable results against source distance variations. Figure 9 shows that the angle error decreases to  $0.5^\circ$  and below after  $d_m > 0.2$  m and  $d_k > 0.3$  m with our proposed solution.

When Figures 7b and 10 are analyzed together, the angle errors decrease down to  $0.1^\circ$  with increasing sampling frequency; at low sampling frequencies, the angle errors in the other two methods increase excessively, while our proposed method has a very small increase compared to the others.

When Figure 11 and Table 1 are analyzed together, our proposed solution for azimuth angle measurement produces more stable results against TDoA measurement errors in the  $0^\circ$ – $90^\circ$  angle range than the other two methods. The results are 41% better than the far-field method and 39.8% better than the other proposed method. When Figure 13 and Table 3 are analyzed for the elevation angle, the success of the three methods is close to each other.

The far-field solution and the other proposed solution require algorithmic inference to determine the quadrant of the DoA. The studies in [21–23] used the tangent function, but they also used algorithmic inference to determine the quadrant. Our proposed solution

produces the correct quadrant result along with the angle information. This eliminates the additional computational cost and provides fast and accurate results.

The field test results support the simulation results. When Tables 4–6 are analyzed, while some TDoA values have errors greater than three samples, the largest azimuth measurement error obtained was less than  $3.5^\circ$ . When analyzing Tables 7 and 8 for the elevation angle, the largest measurement error obtained was  $3.26^\circ$ . These results were within the limits obtained in the simulation studies.

## 6. Conclusions

We have proposed that a closed-form solution is shown to be more successful than existing solutions in simulations. The success of our method in the simulation study is confirmed by the experimental study. The angle error of the existing methods, which is currently close to  $3^\circ$ , is reduced to  $0.5^\circ$  with the appropriate microphone distance. Furthermore, our proposed method eliminates the need for the algorithmic structure used to ascertain the quadrant in which the angle value falls, a requirement present in the other two methods of calculation. The far-field approach results in considerable measurement inaccuracies within the 0 to 30-degree range, causing an unacceptable margin of error in applications like defense and mobile robot positioning. This occurs specifically for sounds emanating from angles within  $\pm 30$  degrees in front of the microphone pair. Our proposed method ensures consistent stability across all angle values. Our solution formula for sensor arrays with co-centered and orthogonally placed geometry has been shown to be more successful for real-time applications.

**Author Contributions:** Methodology, K.Z. and A.Y.; Validation, A.Y.; Writing—original draft, K.Z.; Writing—review & editing, A.Y.; Supervision, A.Y. All authors have read and agreed to the published version of the manuscript.

**Funding:** This research received no external funding.

**Institutional Review Board Statement:** Not applicable.

**Informed Consent Statement:** Not applicable.

**Data Availability Statement:** Not applicable.

**Acknowledgments:** This work is a partial fulfillment of a doctoral study continuing in the Department of Mechatronics Engineering, Graduate School of Science and Engineering at Yildiz Technical University, Istanbul, Türkiye.

**Conflicts of Interest:** The authors declare no conflict of interest.

## References

1. Martin, R.; Heute, U.; Antweiler, C. Acoustic Source Localization with Microphone Arrays. In *Advances in Digital Speech Transmission*; Wiley: Hoboken, NJ, USA, 2008; pp. 135–170. [\[CrossRef\]](#)
2. Brandstein, M.S.; Silverman, H.F. A robust method for speech signal time-delay estimation in reverberant rooms. In Proceedings of the 1997 IEEE International Conference on Acoustics, Speech, and Signal Processing, Munich, Germany, 21–24 April 1997; IEEE: Piscataway, NJ, USA, 1997; Volume 1, pp. 375–378. [\[CrossRef\]](#)
3. Zhuo, D.-B.; Cao, H. Fast Sound Source Localization Based on SRP-PHAT Using Density Peaks Clustering. *Appl. Sci.* **2021**, *11*, 445. [\[CrossRef\]](#)
4. Cobos, M.; Marti, A.; Lopez, J.J. A Modified SRP-PHAT Functional for Robust Real-Time Sound Source Localization with Scalable Spatial Sampling. *IEEE Signal Process. Lett.* **2011**, *18*, 71–74. [\[CrossRef\]](#)
5. Schmidt, R.O. Multiple emitter location and signal parameter estimation. *IEEE Trans. Antennas Propag.* **1986**, *34*, 276–280. [\[CrossRef\]](#)
6. Swindlehurst, A.; Kailath, T. On the sensitivity of the ESPRIT algorithm to non-identical subarrays. *Sadhana* **1990**, *15*, 197–212. [\[CrossRef\]](#)
7. Brandstein, M.; Ward, D. *Microphone Arrays: Signal Processing Techniques and Applications*; Springer Science and Business Media: Medford, OR, USA, 2013.
8. Karbasi, A.; Sugiyama, A. A New Doa Estimation Method Using A Circular Microphone Array. In Proceedings of the 2007 15th European Signal Processing Conference, Poznan, Poland, 3–7 September 2007; pp. 778–782.
9. Boora, R.; Dhull, S.K. A TDOA-based multiple source localization using delay density maps. *Sadhana* **2020**, *45*, 204. [\[CrossRef\]](#)

10. Li, Q.; Zhang, X.; Li, H. Online Direction of Arrival Estimation Based on Deep Learning. In Proceedings of the 2018 IEEE International Conference on Acoustics, Speech and Signal Processing (ICASSP), Calgary, AB, Canada, 15–20 April 2018; pp. 2616–2620. [\[CrossRef\]](#)
11. Xiao, X.; Zhao, S.; Zhong, X.; Jones, D.L.; Chng, E.S.; Li, H. A Learning-Based Approach to Direction of Arrival Estimation in Noisy and Reverberant Environments. In Proceedings of the IEEE International Conference on Acoustics, Speech and Signal Processing (ICASSP), South Brisbane, Australia, 19–24 April 2015; pp. 2814–2818. [\[CrossRef\]](#)
12. Ahmad, M.; Muaz, M.; Adeel, M. A Survey of Deep Neural Network in Acoustic Direction Finding. In Proceedings of the 2021 International Conference on Digital Futures and Transformative Technologies (ICoDT2), Islamabad, Pakistan, 20–21 May 2021; pp. 1–6. [\[CrossRef\]](#)
13. Zhu, M.; Yao, H.; Wu, X.; Lu, Z.; Zhu, X.; Huang, Q. Gaussian filter for TDOA based sound source localization in multimedia surveillance. *Multimedia Tools Appl.* **2018**, *77*, 3369–3385. [\[CrossRef\]](#)
14. Knapp, C.; Carter, G. The generalized correlation method for estimation of time delay. *IEEE Trans. Acoust. Speech Signal Process.* **1976**, *24*, 320–327. [\[CrossRef\]](#)
15. Chung, M.-A.; Chou, H.-C.; Lin, C.-W. Sound Localization Based on Acoustic Source Using Multiple Microphone Array in an Indoor Environment. *Electronics* **2022**, *11*, 890. [\[CrossRef\]](#)
16. Smitha, P.; Elizabeth, S.; Babu, P. Acoustic source localization. *Int. J. Adv. Res. Electr. Electron. Instrum. Eng.* **2013**, *2*, 933–939.
17. Calhoun, R.B.; Dunson, C.; Johnson, M.L.; Lamkin, S.R.; Lewis, W.R.; Showen, R.L.; Sompel, M.A.; Wollman, L.P. Precision and accuracy of acoustic gunshot location in an urban environment. *arXiv* **2021**, arXiv:2108.07377.
18. Ağırman, H.; Karakütük, S.; Gönendik, E. MIKES gunshot detection system prototype. In Proceedings of the 2014 22nd Signal Processing and Communications Applications Conference (SIU), Trabzon, Turkey, 23–25 April 2014; IEEE: Piscataway, NJ, USA, 2014; pp. 2090–2093.
19. Bedard, J.; Pare, S. Ferret: A small arms fire detection system: Localization concepts. In *Sensors, and Command, Control, Communications, and Intelligence (C3I) Technologies for Homeland Defense and Law Enforcement II*; SPIE: Washington, DC, USA, 2003; Volume 5071, pp. 497–509.
20. Jiang, M.; Nnonyelu, C.J.; Lundgren, J.; Thungström, G.; Sjöström, M. A Coherent Wideband Acoustic Source Localization Using a Uniform Circular Array. *Sensors* **2023**, *23*, 5061. [\[CrossRef\]](#) [\[PubMed\]](#)
21. Kundu, T. Acoustic source localization. *Ultrasonics* **2014**, *54*, 25–38. [\[CrossRef\]](#) [\[PubMed\]](#)
22. Ma, C.; Zhou, Z.; Liu, J.; Cui, Z.; Kundu, T. Acoustic source localization using L-shaped sensor clusters: A review. *Ultrasonics* **2023**, *132*, 107020. [\[CrossRef\]](#) [\[PubMed\]](#)
23. Song, P.; Hao, C.; Wu, J.; Yang, C. Acoustic source localization using 10-microphone array based on wireless sensor network. *Sens. Actuators A Phys.* **2017**, *267*, 376–384. [\[CrossRef\]](#)
24. Calderon, D.M.P.; Apolinario, J.A., Jr. Shooter localization based on DoA estimation of gunshot signals and digital map information. *IEEE Lat. Am. Trans.* **2015**, *13*, 441–447. [\[CrossRef\]](#)
25. Imran, M.; Hussain, A.; Qazi, N.M.; Sadiq, M. A methodology for sound source localization and tracking: Development of 3D microphone array for near-field and far-field applications. In Proceedings of the 2016 13th International Bhurban Conference on Applied Sciences and Technology (IBCAST), Islamabad, Pakistan, 12–16 January 2016; pp. 586–591. [\[CrossRef\]](#)
26. Xing, H.; Yang, X. Sound Source Localization Fusion Algorithm and Performance Analysis of a Three-Plane Five-Element Microphone Array. *Appl. Sci.* **2019**, *9*, 2417. [\[CrossRef\]](#)
27. Yang, X.; Xing, H.; Ji, X. Sound Source Omnidirectional Positioning Calibration Method Based on Microphone Observation Angle. *Complexity* **2018**, *2018*, 2317853. [\[CrossRef\]](#)
28. Nal, E.; Kayaoğlu, M.; Topçu, B.; Doğan, M.U. An acoustic based sniper detection system prototype. In Proceedings of the 2011 IEEE 19th Signal Processing and Communications Applications Conference (SIU), Antalya, Turkey, 20–22 April 2011; IEEE: Piscataway, NJ, USA, 2011; pp. 311–314.
29. Parsayan, A.; Ahadi, S.M. Real Time High Accuracy 3-D PHAT-Based Sound Source Localization Using a Simple 4-Microphone Arrangement. *IEEE Syst. J.* **2011**, *6*, 455–468. [\[CrossRef\]](#)
30. Smith, J.O.; Abel, J.S. Closed-form least-squares source location estimation from range-difference measurements. *IEEE Trans. Acoust. Speech Signal Process.* **1987**, *35*, 1661–1669. [\[CrossRef\]](#)

**Disclaimer/Publisher’s Note:** The statements, opinions and data contained in all publications are solely those of the individual author(s) and contributor(s) and not of MDPI and/or the editor(s). MDPI and/or the editor(s) disclaim responsibility for any injury to people or property resulting from any ideas, methods, instructions or products referred to in the content.